Nano Energy 76 (2020) 104944

Contents lists available at ScienceDirect

Nano Energy

journal homepage: http://www.elsevier.com/locate/nanoen

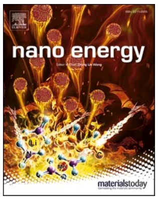

Ultrahigh piezoelectricity in lead-free piezoceramics by synergistic design

Dawei Wang [a,*,1], Zhongming Fan [b,1], Guanghui Rao [c,1], Ge Wang [a,1], Yao Liu [d,1], Changlai Yuan [c], Tao Ma [e], Dejun Li [f], Xiaoli Tan [b], Zhilun Lu [a], Antonio Feteira [g], Shiyu Liu [f,**], Changrong Zhou [c,***], Shujun Zhang [h,****]

[a] Department of Materials Science and Engineering, University of Sheffield, Sheffield, S1 3JD, UK
[b] Department of Materials Science and Engineering, Iowa State University, Ames, IA, 50011, USA
[c] Guangxi Key Laboratory of Information Materials, School of Material Science and Engineering, Guilin University of Electronic Technology, Guilin, Guangxi, 541004, China
[d] Electronic Materials Research Lab, Key Lab of Education Ministry/International Center for Dielectric Research, School of Electronic and Information Engineering, Xi'an Jiaotong University, Xi'an, 710049, China
[e] Ames Laboratory, U.S. Department of Energy, Ames, IA, 50011, USA
[f] College of Physics and Materials Science, Tianjin Normal University, Tianjin, 300387, China
[g] Christian Doppler Lab on Advanced Ferroic Oxides, Materials and Engineering Research Institute, Sheffield Hallam University, Sheffield, S1 1WB, UK
[h] Institute for Superconducting and Electronic Materials, Australian Institute for Innovative Materials, University of Wollongong, Wollongong, NSW, 2500, Australia

ARTICLE INFO

Keywords:
Lead-free ceramics
Piezoelectrics
Dielectrics
$BaTiO_3$

ABSTRACT

Following increased environmental concerns on the toxicity of lead, the discovery of ultrahigh piezoelectricity in lead-free piezoelectric materials is critical for the substitution of commercial lead zirconate titanate (PZT) ceramics in numerous electronic devices. In this work, a synergistic design strategy is proposed to enhance the piezoelectricity in lead-free piezoelectric materials by flattening the Gibbs free energy density profile, via the coexistence of multiple phases and local structural heterogeneity. This strategic material design approach is based on first-principles calculations combined with Landau phenomenological theory and phase field simulations. Sustainable Stannum-doped $BaTiO_3$ lead-free ferroelectric ceramics are prepared to validate our proposed mechanism, and a giant piezoelectric coefficient $d_{33} > 1100$ pC/N is achieved, being the highest value reported in lead-free piezoceramics. The mechanism and paradigm of the excellent piezoelectricity achieved here provides a feasible solution for replacing lead-based piezoelectrics by lead-free counterparts.

1. Introduction

Piezoelectric materials convert mechanical stress to electric charge and vice-versa. This phenomenon originally demonstrated by the Curie brothers in 1880, has been vital for the successful operation of many advanced electronic devices such as micropositioning actuators, piezoelectric sensors, ultrasonic imaging transducers, to name a few [1–3]. For over sixty years, the piezoelectric materials market has been dominated by lead zirconate titanate $Pb(Zr,Ti)O_3$-based ceramics (PZTs), because they offer the best affordable combination of piezoelectric characteristics, i.e. the largest magnitude of piezoelectric coefficient (*d*), electromechanical coupling (*k*) and temperature stability. The excellent piezoelectric properties of ferroelectric PZT perovskite have been ascribed to the coexistence of rhombohedral (R) and tetragonal (T) phases at a morphotropic phase boundary (MPB) [1–3].

In the late 20th century, due to an ever increasing awareness of the hazardous effects of lead to human health and environment, its use became a subject of legal restrictions, such as the Restriction of Hazardous Substances Directive (RoHS) (2003) by the European Union, which particularly limits the usage of lead in electronic devices [4]. This prompted the search and development of lead-free piezoelectric ceramics which could be effective alternatives to PZTs [5–7], however, to

---

* Corresponding author.
** Corresponding author.
*** Corresponding author.
**** Corresponding author.

E-mail addresses: dawei.wang@sheffield.ac.uk (D. Wang), buaasyliu@gmail.com (S. Liu), zcr750320@guet.edu.cn (C. Zhou), shujun@uow.edu.au (S. Zhang).

[1] Author contributions: These authors contributed equally to this work.

https://doi.org/10.1016/j.nanoen.2020.104944
Received 25 March 2020; Received in revised form 8 April 2020; Accepted 18 April 2020

date there is no lead-free piezoelectric able to totally replace PZTs. There are a number of potential candidates such as (K,Na)NbO$_3$ (KNN), Bi$_{1/2}$Na$_{1/2}$TiO$_3$ (BNT), (Ba,Ca)(Zr,Ti)O$_3$ (BCZT) and BiFeO$_3$–BaTiO$_3$ (BF-BT), each of which exhibits strengths and weaknesses [8–12]. Extensive research on KNN based materials was originally triggered by Saito et al., in 2004, reporting textured (K$_{0.44}$Na$_{0.52}$Li$_{0.04}$)(Nb$_{0.86}$Ta$_{0.10}$Sb$_{0.04}$)O$_3$ ceramics with Curie temperature (T_C) of 253 °C and high piezoelectric coefficient (d_{33}) = 416 pC/N [13–19]. Later, Liu and Ren reported an even higher d_{33} of 620 pC/N for 0.50Ba(Zr$_{0.2}$Ti$_{0.8}$)O$_3$-0.50(Ba$_{0.7}$Ca$_{0.3}$)TiO$_3$ (BZT-50BCT) [20], which in that case was ascribed to the occurrence of a tri-critical point (TCP) consisting of T, R and cubic (C) phases. In 2015, Lee et al. reported a R-T MPB in quenched BF-BT with both high d_{33} (240–402 pC/N) and T_C (>400 °C) [21].

A comparison of d_{33} *vs* T_C/T_m (where T_m is the temperature of maximum dielectric permittivity) for lead-based and lead-free piezoelectric ceramics is plotted in Fig. 1a [8–12]. Generally, the values of d_{33} decrease with the increase of T_C/T_m, but clearly lead-based ceramics exhibit much larger d_{33} values than lead-free ceramics, which is still the main factor limiting the commercialization of lead-free ceramics. Recently, a new material design approach based on flattening the thermodynamic energy profile of ferroelectrics by local structural heterogeneity allowed to circumvent this so-called "ceiling effect" on high piezoelectricity in lead-free materials (Fig. 1a). Indeed, this design approach was successfully applied to improve piezoactivity in Sm-doped Pb(Mg$_{1/3}$Nb$_{2/3}$)O$_3$–PbTiO$_3$ (PMN-PT) ceramics (d_{33} > 1500 pC/N) and single-crystals (d_{33} ~ 4000 pC/N), [22,23]. Consequently, this has widened further the piezoelectric performance gap between lead and lead-free materials.

2. Results and discussion

2.1. A synergistic strategy for high piezoelectricity: design, calculation and simulation

According to the Landau phenomenological theory [22–26,46], a high d_{33} can be obtained via flattening of the Gibbs free-energy density profile with respect to polarization. This can be achieved either by a macroscopic coexistence of multiple phases (CMP) or by microscopic local structural heterogeneity (LSH). In principle, a combination of both mechanisms (CMP and LSH) can induce a greater enhancement of the intrinsic d_{33}, which to our knowledge has not yet been reported in lead-free materials.

A synergistic approach combining CMP and LSH was designed, and tried to break the high piezoelectricity "ceiling effect" in lead-free ceramics. In order to demonstrate the feasibility and significance of this approach, we selected Sn-doped BaTiO$_3$ (BT), as it contains no volatile or scarce elements. On cooling, the crystal structure of BT successively changes from C, T, O to R, as shown in Fig. S1 (Supplemental Information). The C phase is a nonpolar phase, while T, O and R phases are polar phases with polarization vectors along [100], [101] and [111], respectively. Mathematically, the [100], [101] and [111] polarization vectors form a complete set of base vectors that spatially can express/represent any polarization vector under special stimuli conditions. Hence, CMP of T, O, R and C provides an ideal arrangement due to its mathematical completeness. This allows the construction of a four-phase CMP, which one could expect to provide the flattest thermodynamic energy profile and therefore enhanced piezoelectricity. From a mathematical viewpoint, complex multiple states with [100], [101], [111] polarization vectors and origin point at [000], corresponding to T, O, R and C phases, respectively, are preferred.

In this work, first-principles calculations combined with Landau free-energy theory are employed to realize the design of CMP in lead-free Sn-doped BT ceramics (BaTi$_{1\text{-}x}$Sn$_x$O$_3$, BTS*x*, $0 \leq x \leq 0.2$), which was strategically chosen to verify the feasibility of the aforementioned proof-of-concept. The total-energy (E) of T, O, R and C phase for BTS*x* was calculated separately by first-principles calculations, and the corresponding total-energy difference ($\Delta E = E_i\text{-}E_C$, i = T, O, R) between T, O, R and C phase as a function of Sn concentration is shown Fig. 1b. For pure BT, the order of structural stability is R > O > T > C, in agreement with the experimental observation of C-T-O-R phase transition upon cooling (Fig. S1, Supplemental Information). With increasing Sn content, ΔE between R, T, O and C phases is found to decrease continuously, reaching zero at $x \geq 0.11$, suggesting the coexistence of R, T, O and C phases. This is further corroborated by the convergence of the calculated lattice parameters and volumes for different phase structures in BTS*x* (Fig. S2a, Supplemental Information). In order to further appraise the proof-of-concept, ΔE values, lattice parameters and volumes of Ba$_{1\text{-}x}$Ca$_x$TiO$_3$ (BC*x*T), BaZr$_x$Ti$_{1\text{-}x}$O$_3$ (BZ*x*T) and PbZr$_x$Ti$_{1\text{-}x}$O$_3$ (PZ*x*T) were calculated from first-principles calculations and compared in Fig. 1b and Fig. S2 (Supplemental Information). Although BZ*x*T and BTS*x* show similar CMP, i.e. R, O, T and C phases coexisting at x > 0.20, T_C of BZ*x*T (x > 0.20) is below room temperature resulting in no piezoactivity at room temperature [2,27]. Furthermore, the total energy of C phase for BC*x*T and PZ*x*T is always higher than that of R, O, T phases. Calculated lattice parameters and volumes never converge (Fig. S2, Supplemental Information), ruling out coexistence of R, O, T and C phases in BC*x*T and

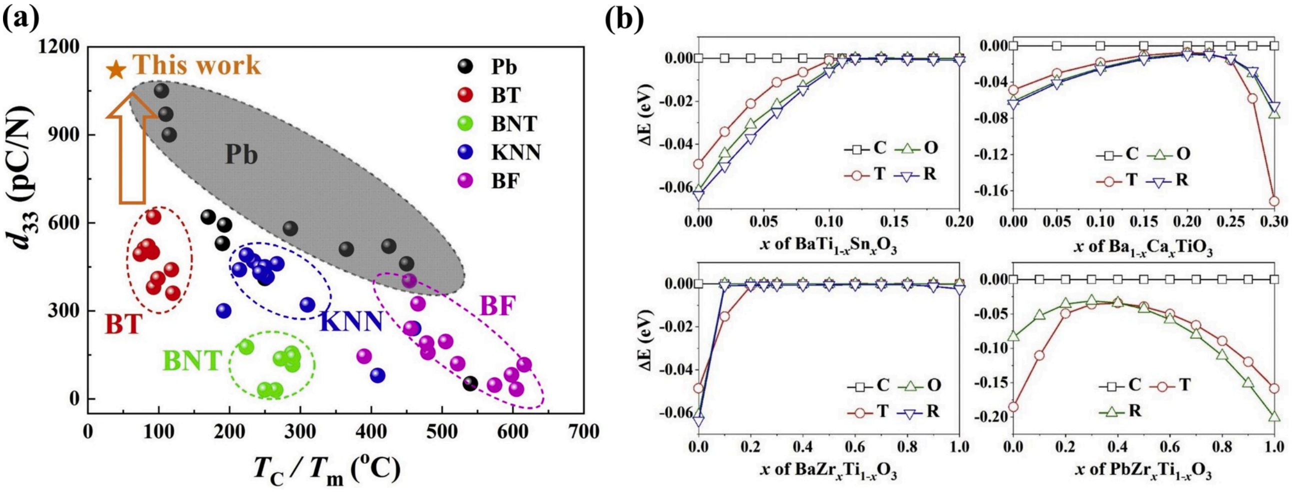

Fig. 1. (a) A comparison of d_{33} *vs* T_C/T_m for piezoelectric ceramics. (b) The calculated the total-energy difference per unit cell ($\Delta E = E_i - E_C$, E_i: total energy of T, O and R phases; E_C: total energy of C phase) of C, T, O and R BaTi$_{1\text{-}x}$Sn$_x$O$_3$ ($0 \leq x \leq 0.2$), Ba$_{1\text{-}x}$Ca$_x$TiO$_3$ ($0 \leq x \leq 0.3$), BaZr$_x$Ti$_{1\text{-}x}$O$_3$ ($0 \leq x \leq 1$) and PbZr$_x$Ti$_{1\text{-}x}$O$_3$ ($0 \leq x \leq 1$).

PZ*x*T, in contrast with BZ*x*T and BTS*x*.

On the other hand, ferroelectrics may evolve into relaxor ferroelectrics (RFEs) by an increase of LSH, which is accompanied by the appearance of numerous polar nanoregions (PNRs) embedded in a non-polar matrix [28]. Due to the similar total energies between the non-polar phase (C) and the polar phases (R, O, T) in BTS*x* ($x \geq 0.11$, Fig. 1b), PNRs with multiple crystal symmetries (T, O, R) can be randomly nucleated, formed and embedded in the non-polar (C) matrix, which will have different polarization directions, as demonstrated by phase-field simulations shown in Fig. 2a,b. This arrangement of PNRs appears to be isotropic and macroscopically paraelectric (system with zero macroscopic polarization), which is consistent with the super-paraelectric model [29]. The Landau free-energy profile for polarization rotation of BTS*x* is shown in Fig. 2d. The spherical surface of the Landau free-energy in the polarization space suggests that the polar T, O and R phases may readily undergo rotation among the corresponding [100], [101] and [111] polarization directions (Fig. 2d,e). The Landau free-energy profile of polarization extension for different polarization directions further indicates a low-barrier and nearly-free extension of the polarization direction (Fig. 2f). Therefore, these multiphasic (T, O, R) PNRs in BTS*x* are easily re-orientable, re-extended and orderly re-arranged upon the application of a small external electric field (Fig. 2c), which is expected to lead to high piezoelectricity.

2.2. Structure and piezoelectricity of Sn-doped BT ceramics

Room temperature XRD patterns of BTS*x* in the 2θ range of 20°~70° are shown in Fig. S3 (Supplemental Information) and several expanded diffraction peaks are given in Fig. 3a. Peaks are ascribed to either a single-phase perovskite or a mixture of perovskite phases, without any detectable secondary impurity phases. The shift of the diffraction peaks towards lower 2θ with increasing Sn content is consistent with the replacement of Ti^{4+} (0.605 Å) by the larger Sn^{4+} (0.69 Å) [47]. Furthermore, the expanded XRD patterns (Fig. 3a) reveal an apparent coexistence of multiple symmetries at room-temperature for $x \leq 0.14$, as corroborated by the broadening of peaks. Full pattern Rietveld refinement was performed for all compositions, as shown in Fig. S3 (Supplemental Information), using orthorhombic (O, *Amm2*), tetragonal (T, *P4mm*), rhombohedral (R, *R3m*) and cubic (C, $Pm\overline{3}m$) phases, the corresponding results are listed in Fig. 3b and Table S1 (Supplemental Information). A mixture of O (68%) and T (32%) phase is refined for $x = 0.05$, yielding an excellent good of fitness (GOF) ~ 1.86. With the increase of Sn concentration, a higher amount of T (53%) phase (O phase ~ 47%) is found at $x = 0.08$. Coexistence of four phases (C, T, R and O) is observed in $x = 0.11$. The fraction of dominant C phase (86% for $x = 0.14$) increases continuously and becomes the sole phase $x = 0.18$. The coexistence of crystal symmetries as determined from refinement of the X-ray data agrees with results gathered by a combination of other techniques. For example, the gradual decrease in T phase content with increasing x and its complete absence in $x = 0.14$ is commensurate with the disappearance of the sharp mixed mode $E(LO_2 + TO_3) + B_1$ at 303 cm^{-1} from the Raman spectra as shown in Fig. S4 (Supplemental information) [30]. The presence of R is consistent with a residual $A_1(TO)$ mode at 185 cm^{-1}, but also it is expected from evolution of the permittivity behavior as depicted in Fig. 3c,d. The occurrence O symmetry is difficult to ascertain from the Raman data, however it is readily discerned from the high-resolution scanning transmission electron microscopy (HRSTEM) images, as shown later in Fig. 5 for $x = 0.11$. The C phase expected far above the permittivity maximum, is an average structure, because the occurrence of modes in the Raman spectra is sufficient to rule out a truly centrosymmetric symmetry.

A continuous phase transition can also be clearly observed in the temperature dependence of dielectric permittivity (ε_r) and loss (tan δ), as shown in Fig. 3c and Fig. S5 (Supplemental Information). It is clear that with the increase of Sn content, T_m is found to decrease linearly from 87 °C for $x = 0.05$ to −17 °C for $x = 0.18$, with a gradual pinching of both phase transition temperatures of R to O phase ($T_{R\text{-}O}$) and O to T phase ($T_{O\text{-}T}$) close to room temperature (Fig. 3d). Based on the results of XRD and temperature dependence of ε_r and tan δ, a phase diagram of BTS*x* as function of Sn concentration is schematically plotted, as shown in Fig. 3d, which clearly indicates that four phases, C, T, R and O, coexist near room temperature, in consistent with the DFT calculation (Fig. 1b),

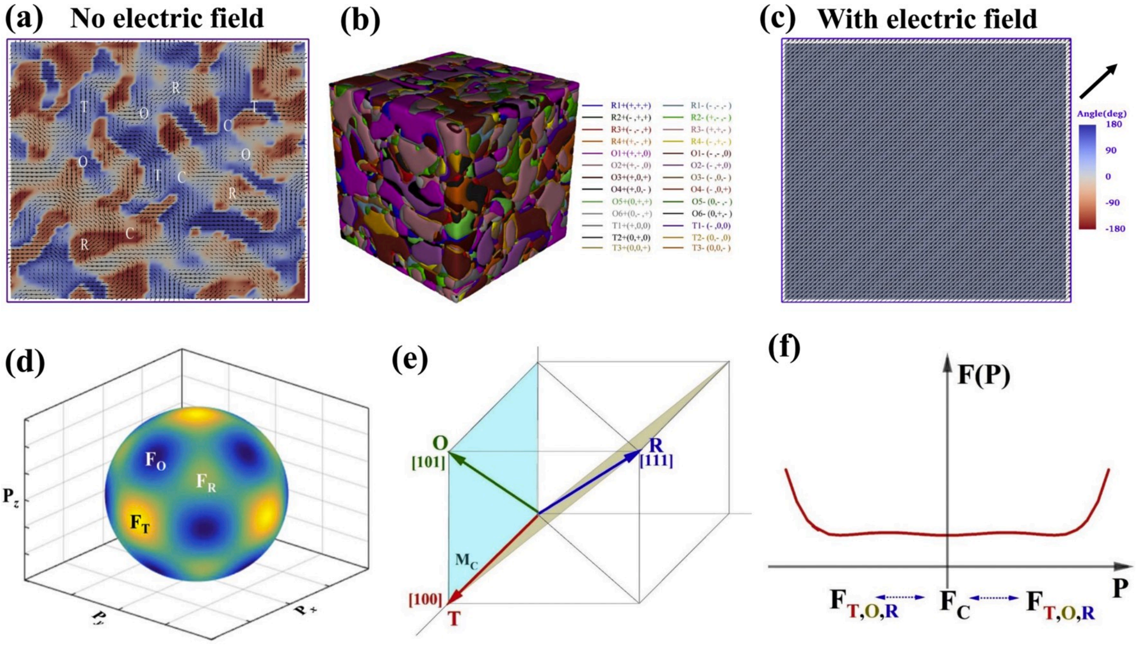

Fig. 2. (a) Phase-field simulation of two-dimensional domain structure of RFEs with PNRs in nonpolar C phase without an external electric field. (b) Phase-field simulation of three-dimensional schematic of domain structure without an external electric field. (c) Phase-field simulation of two-dimensional domain structure of RFEs with an external electric field. (d) Three-dimensional schematic for the Landau free-energy profile of polarization rotation of RFEs for different polarizations within Landau theory under a four-phase coexistence condition. (e) Schematic of the respective [100], [101], and [111] polarization directions for the T, O, and R phases, respectively. (f) The Landau free-energy profiles of polarization extension for different polarization directions.

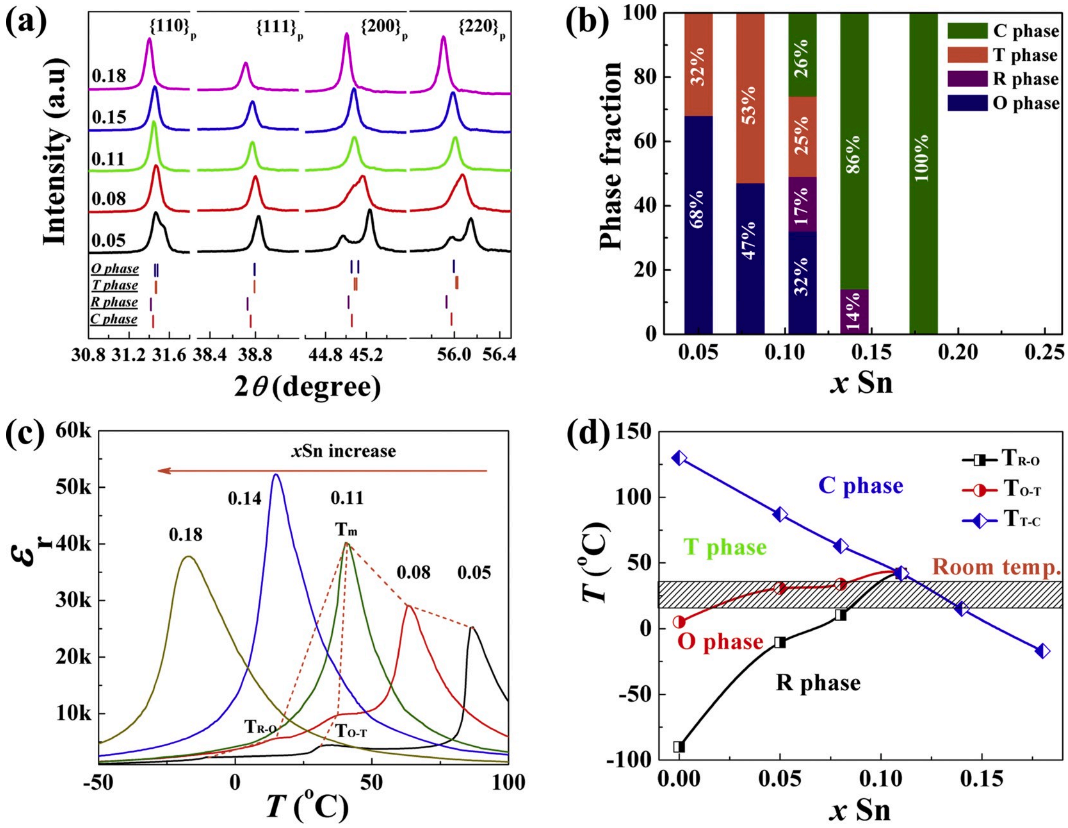

Fig. 3. (a) Enlarged $\{110\}_p$, $\{111\}_p$, $\{200\}_p$ and $\{220\}_p$ peaks in the XRD patterns of BTS*x*. (b) phase fraction in BTS*x* as a function of *x*. (c) temperature dependence of dielectric permittivity (ε_r) for BTS*x*. (d) phase diagram of BTS*x* as function of *x*.

Landau free-energy profile (Fig. 2d,f) and XRD results (Fig. 3a and b). The relaxor behavior of BTS*x* is analyzed using the modified Curie-Weiss law and the corresponding results are plotted in Fig. S6 (Supplemental Information). The degree of diffuseness (γ) is found to increase from 1.42 for $x = 0.05$ to 1.80 for $x = 0.18$, indicative of an enhanced relaxor behavior by Sn doping, in agreement with the Landau phenomenological theory and phase field simulation (Fig. 2).

The d_{33} and planar eletromechanical coupling constant (k_p) of BTS*x* ceramics as function of *x* are shown in Fig. 4a. It is clear that values of d_{33} and k_p for BTS*x* ceramics are significantly enhanced by Sn doping, with the maximum values of $d_{33} \sim 1120$ pC/N and $k_p \sim 0.55$ achieved at $x = 0.11$. Furthermore, the maximum piezoelectric strain coefficient *dS/dE*, quasi-static positive and negative maximum d_{33} (d_{33}^{Emax} and -d_{33}^{Emax}) exhibit even larger values of 1700, 2180 and 1720 p.m./V (Fig. 4b and c), respectively, further confirming the ultrahigh piezoelectricity. On the other hand, the *ex-situ* temperature dependence of d_{33} and k_p for BTS*x* ($x = 0.11$) indicates that the piezoelectricity is stable until T_m is reached, above which it drops dramatically (Fig. 4d), which is also further confirmed by the *in-situ* temperature dependence of *dS/dE*, d_{33}^{Emax} and -d_{33}^{Emax} (Fig. 4e and f). Room temperature d_{33} of BTS_x ($x = 0.11$) is compared with that of other lead-free piezoelectrics and several typical PZT compositions and given in Fig. 4g,h. Our giant d_{33} value of ~1120 pC/N is about twice that of other BT-based, KNN-based systems and soft PZTs encompassing only R + T or R + O + T mixed phases, such as 620 pC/N for BTZ-0.5BCT (Fig. 4g) [20], 570 pC/N for $0.95K_{0.6}Na_{0.4}Nb_{0.965}Sb_{0.035}O_3$-$0.02BaZrO_3$-$0.03Bi_{0.5}K_{0.5}HfO_3$ (Fig. 4h) [15] and 590 pC/N for ultrasoft PZT5H (Fig. 4h) [31], which is currently the highest value reported in lead-free materials.

Fig. 5 displays the microstructure of BTS*x* ($x = 0.11$). No micron-sized domains exist in the grain (Fig. 5a), which is in consistence with the relaxor nature of BTS*x* ($x = 0.11$) (Fig. S6, Supplemental Information). In order to examine whether the structural heterogeneity, if any, is attributed to the chemical inhomogeneity, the energy dispersive X-ray (EDX) mapping was carried out in a very small area shown in Fig. 5b. All four elements appear to be uniformly distributed, excluding any possible role played by the chemical segregation. Furthermore, the dipoles are mapped out based on the same HRSTEM micrograph, as shown in Fig. 5c. As explained earlier, R, T and O phases feature different polarization directions. The left portion in Fig. 5c with dipoles pointing to <110> could be an O domain, while the right portion having dipoles aligned along <100> direction is most likely to be T phase. It should be noted that the left nano-domain might also be R since the polar vectors in R and O are indiscernible under <001> zone axis. Nevertheless, a O phase is more likely because in this particular composition its phase fraction is almost twice that of R phase (Fig. 3b). The region between the two nano-domains should be regarded as a domain boundary, which is also an inter-phase interface.

3. Conclusions

This work provides a new methodology and feasible solution to design materials with a record high piezoelectric coefficient among lead-free piezoelectrics. The first-principles calculations combined with Landau phenomenological theory and phase field simulation are powerful tools to design, calculate and simulate compositions, crystal structures, microstructures, energies etc. in ferroelectrics, with respect to different material systems and dopants. Indeed, a giant piezoelectric coefficient $d_{33} > 1100$ pC/N is achieved in Sn-doped $BaTiO_3$ (BTS_x) ($x = 0.11$) ceramics, which is the highest value reported for lead-free ceramics. This remarkable enhancement of the piezoelectricity can be ascribed to the strategic design of a flat Gibbs free energy density profile via a synergistic approach that involves both coexistence of multiple phases (CMP) and local structural heterogeneity (LSH). The occurrence of these two mechanisms is confirmed by crystal structure,

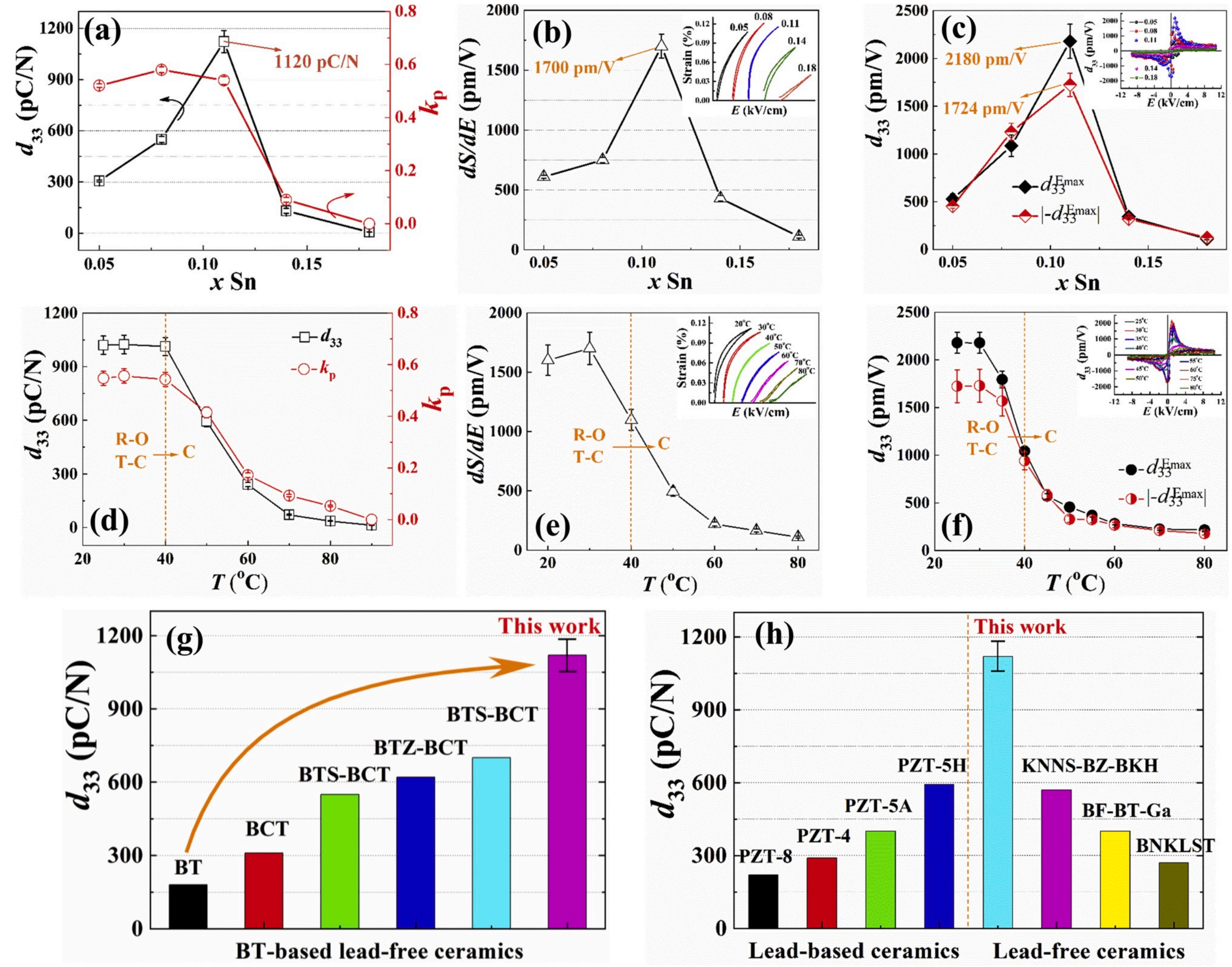

Fig. 4. (a) The piezoelectric coefficient d_{33} and the planar eletromechanical coupling coefficient k_p. (b) the unipolar strain *vs.* electric field (*S-E*) loops and corresponding maximum converse piezoelectric coefficient dS/dE. (c) bias field d_{33}* *vs.* electric field (d_{33}*-*E*) hysteresis loops and corresponding quasi-static positive and negative maximum d_{33} (d_{33}^{Emax} and -d_{33}^{Emax}) of BTS*x* ceramics as function of *x*. The temperature dependence of (d) d_{33} and k_p, (e) *S-E* loops and dS/dE, (f) d_{33}*-*E* loops, d_{33}^{Emax} and -d_{33}^{Emax}. The comparison in the room temperature d_{33} of BTS*x* ($x = 0.11$) with (g) BT-based piezoelectrics [20,31–35] and (h) several typical PZT and lead-free piezoelectrics [14–17,21,36].

microstructure and property characterization of BTS_x ceramics. Hence this synergistic approach that combines macroscopically CMP with microscopically LSH may pave the way to halt the dominant role of lead-based ceramics in piezoelectric applications. Moreover, we would like to emphasize that the proposed strategy to enhance the piezoelectricity is not limited to ferroelectrics but could be further generalized to use for understanding and optimizing a wide range of functionalities.

4. Experimental

4.1. Sample preparation

$Ba(Ti_{1-x}Sn_x)O_3$+0.6% MnO_2 (x = 0.05, 0.08, 0.11, 0.14, and 0.18) ceramics were prepared by the conventional solid-state reaction method, where MnO_2 is used to reduce to conductivity. Dried high purity raw materials of TiO_2 (99.95%), SnO_2 (99.9%), $BaCO_3$ (99.9%) and MnO_2 (99%) were weighed stoichiometrically and ball-milled in an ethanol solvent using yttria-stabilized zirconia medium for 24 h. Subsequently, the dried mixture was ground and calcined at 1150 °C for 4 h, followed by further milling for 16 h. Powders were dried, mixed with 6 wt% polyvinyl alcohol (PVA) and then pressed into pellets of 12 mm in diameter and 1 mm in thickness under a uniaxial pressure of 80 MPa. Green pellets were sintered at 1380 °C for 4 h in air after binder burn-out at 550 °C. Surfaces of as-sintered ceramics were ground and silver paste electrode was applied and fired at 600 °C for 10 min. The electric poling was carried out by applying a dc field of 4 kV/mm for 10 min in a silicone oil bath.

4.2. Characterization

The crystal structure of crushed and ground ceramic powder was analyzed by X-ray diffraction (XRD, Bruker D2 Phaser, Germany) with a Cu Kα radiation. Full-pattern Rietveld refinement was carried out using TOPAS 5 to obtain phase fraction and crystallographic information. An FEI Titan Themis 300 probe-corrected scanning transmission electron microscopy (STEM) operated at an accelerating voltage of 200 kV, equipped with a Super-X energy dispersive X-ray spectroscopy (EDX) detector, was employed for TEM observation and EDX acquisition. High-angle annular dark-field (HAADF) images were captured using a sub-angstrom electron probe with a convergence angle of 18 mrad and a detection angle of 99–200 mrad. The atomic positions of both A-site and B-site columns were determined by fitting the intensity maxima in these images using a 2D Gaussian function. The off-center displacements of Ti cations were calculated with respect to the geometric center of the four

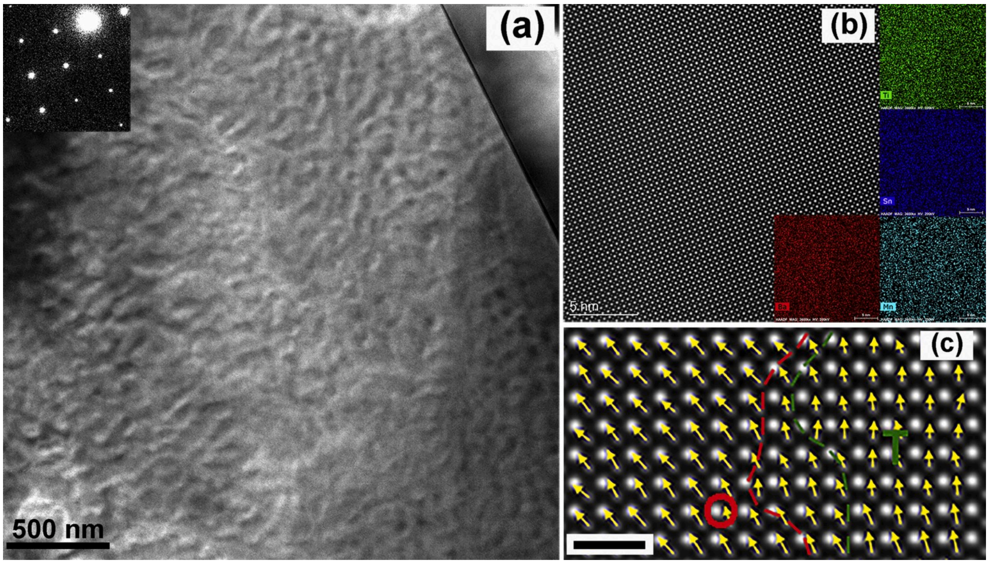

Fig. 5. (a) Bright-field TEM micrograph of the domain structure in BTSx ($x = 0.11$) observed along <001> zone axis. (b) EDX mapping of Ba, Ti, Sn and Mn based on the HAADF-STEM image. (c) Ti cation displacement mapping within two neighboring domains. The scale bar measures 1 nm.

surrounding A-site columns and overlaid on the HAADF images. The detailed description of the homemade code can be found elsewhere [37]. The piezoelectric coefficient (d_{33}) of poled pellets was measured by a Berlincourt meter (ZJ-3A, China). The planar electromechanical coupling coefficient k_p and dielectric properties was measured by a precision impedance analyzer (HP 4294A, Agilent, USA) under a temperature range of -50 to 150 °C. A ferroelectric tester system (TF Analyzer, 2000HS, aixACCT Systems GmbH, Aachen, Germany) was employed for the ferroelectric, piezoelectric and strain measurements, including electric-field induced unipolar/bipolar strain (S-E), polarization (P-E) hysteresis loops and bias field $d_{33}{}^*(E)$ hysteresis loops (AC signal of 10 V at 250 Hz).

4.3. First-principles calculations

The first-principles calculations were carried out based on density functional theory (DFT), the pseudopotential method, and plane-wave basis sets [38,39]. The results reported in this paper were obtained with the use of the Cambridge serial total energy package (CASTEP) [40]. The exchange-correlation effects were treated with the generalized gradient approximation (GGA) [41]. For the modeling of the $BaTi_{1-x}Sn_xO_3$ ($0 \leq x \leq 0.2$) solid solutions, we have adopted the virtual crystal approximation (VCA), which implies preserving the same crystalline unit cells as $BaTiO_3$ and replacing the transition metal Ti with a virtual Sn atom [42,43]. A plane-wave cutoff energy of 800 eV was employed in the calculations, which assured a total energy convergence of 10^{-6} eV/atom. For the bulk calculations in which primitive unit cells were employed, the Brillouin zone sampling was set with the $8 \times 8 \times 8$ Monkhorst-Pack k-points meshes. All the primitive unit cells were allowed to fully relax until the force on each atom was smaller than 0.01 eV/Å.

4.4. Landau free energy modeling within our multiphase model from first-principles

To analyze the high electromechanical properties of the relaxor within our multiphase coexistence model, we employ Landau-Devonshire (LD) theory within the 6th-order terms of polarization. The free energy of a ferroelectric can be written in terms of the polarization components (P_x, P_y, P_z) as follows [41–43[46]].

$$\begin{aligned} F(\overrightarrow{P}) = {} & F_0 + \alpha\left(P_x^2 + P_y^2 + P_z^2\right) + \beta_1\left(P_x^4 + P_y^4 + P_z^4\right) \\ & + \beta_2\left(P_x^2P_y^2 + P_y^2P_x^2 + P_z^2P_x^2\right) + \gamma_1\left(P_x^6 + P_y^6 + P_z^6\right) \\ & + \gamma_2\left[P_x^4\left(P_y^2 + P_z^2\right) + P_y^4\left(P_z^2 + P_x^2\right) + P_z^4\left(P_x^2 + P_y^2\right)\right] + \gamma_3 P_x^2P_y^2P_z^2, \end{aligned} \tag{1}$$

where parameters α, β_1, β_2, γ_1, γ_2, and γ_3 are the coefficients of different orders of polarization $\boldsymbol{P}$. $F(\overrightarrow{P})$ represents the free energy at a certain temperature and composition as a function of polarization. F_0 denotes the free energy of a paraelectric phase. For our multiphase model for four-phase coexistence with the tetragonal (T), rhombohedral (R), orthorhombic (O), and cubic (C) phases, the free energy of each phase is the same, and the first deviation of the free energy for a certain phase is zero in order to make the phase stable. For simplicity, we assume that polarizations in three different ferroelectric phases have the same length but with different orientations, and we can then write

$$F(\overrightarrow{P_T}) = F(\overrightarrow{P_O}) = F(\overrightarrow{P_R}) = F(\overrightarrow{P_C}) = F_0, \tag{2}$$

$$\text{and } dF(\overrightarrow{P})/d(\overrightarrow{P}) = 0 \text{ (at } \overrightarrow{P} = \overrightarrow{P_T}, \overrightarrow{P} = \overrightarrow{P_R}, \overrightarrow{P} = \overrightarrow{P_O}) \tag{3}$$

where $\overrightarrow{P_T} = P_0{}^*(0, 0, 1), \overrightarrow{P_R} = P_0{}^*\left(\frac{1}{\sqrt{3}}, \frac{1}{\sqrt{3}}, \frac{1}{\sqrt{3}}\right), \overrightarrow{P_O} = P_0{}^*\left(0, \frac{1}{\sqrt{2}}, \frac{1}{\sqrt{2}}\right)$

Based on Eqs. (2) and (3), the free energy can be rewritten as

$$F(\overrightarrow{P}) = F_0 + \gamma_1 P_0^4 P^2 - 2\gamma_1 P_0^2 P^4 + \gamma_1 P^6, \tag{4}$$

4.5. Phase field simulations

In phase field simulations a ferroelectric system with local phase fluctuation [44], the temporal evolution of a polarization field is described by the Time-Dependent Ginzburg-Landau (TDGL) equation,

$$\frac{\partial P_i(\mathbf{r}, t)}{\partial t} = -L\frac{\delta F}{\delta P_i(\mathbf{r}, t)}, (i = 1, 2, 3), \tag{5}$$

where L is the kinetic coefficient, F, the total free energy of the system, $\mathbf{r}$, space position, and P_i ($\mathbf{r}$, t) is the polarization. $\delta F/\delta P_i$ ($\mathbf{r}$, t) is the thermodynamic driving force for the spatial and temporal evolution of δP_i (**r**, t). The total free energy of the system includes the bulk free energy, elastic energy, electrostatic energy, and the gradient energy:

$$F=\int_V\left[f_{\text{bulk}}+f_{\text{elas}}+f_{\text{elec}}+f_{\text{grad}}\right]dV \tag{6}$$

where V is the system volume, f_{bulk} denotes the Landau bulk free energy density, f_{elas} the elastic energy density, f_{elec} the electrostatic energy density and f_{grad} the gradient energy density. The bulk free energy density is expressed by Landau theory as

$$\begin{aligned}f_{\text{bulk}}=&\alpha_1\left(P_1^2+P_2^2+P_3^2\right)+\alpha_{11}\left(P_1^4+P_2^4+P_3^4\right)+\alpha_{12}\left(P_1^2P_2^2+P_2^2P_3^2+P_3^2P_1^2\right)\\&+\alpha_{111}\left(P_1^6+P_2^6+P_3^6\right)+\alpha_{112}\left[\left(P_1^4\left(P_2^2+P_3^2\right)+P_2^4\left(P_1^2+P_3^2\right)+P_3^4\left(P_1^2+P_2^2\right)\right]\\&+\alpha_{123}P_1^2P_2^2P_3^2\end{aligned} \tag{7}$$

where α_1, α_{11}, α_{12}, α_{111}, α_{112} and α_{123} are Landau energy coefficients. The values of these coefficients determine the thermodynamic behaviors of the bulk phases. Based on experimental data (phase transition temperatures and dielectric properties), the Landau coefficients of BST (x = 0–0.2) are set to be:

$\alpha_1 = 2.34 \times 10^5\ (T\text{-}381 + 700x)\ C^{-2}m^2N$,
$\alpha_{11} = 4.69 \times 10^6(T\text{-}393 + 700x)\text{-}2.18 \times 10^8\ C^{-4}m^6N$,
$\alpha_{12} = 1.83 \times 10^8\ C^{-4}m^6N$,
$\alpha_{111} = \text{-}6.52 \times 10^7(T\text{-}393 + 700x)+2.96 \times 10^9\ C^{-6}m^{10}N$,
$\alpha_{112} = 1.77 \times 10^8\ C^{-6}m^{10}N$,
$\alpha_{123} = 1.\ 3 \times 10^8\ C^{-6}m^{10}N$.

The parameters in the elastic, electrostatic and gradient energy density are assumed to be uniform throughout the system [45]. The gradient energy density, associated with the formation and evolution of domain walls, can be expressed as

$$\begin{aligned}f_{\text{grad}}=&\frac{1}{2}G_{11}\left(P_{1,1}^2+P_{2,2}^2+P_{3,3}^2\right)+G_{12}(P_{1,1}P_{2,2}+P_{2,2}P_{3,3}+P_{1,1}P_{3,3})\\&+\frac{1}{2}G_{44}\left[(P_{1,2}+P_{2,1})^2+(P_{2,3}+P_{3,2})^2+(P_{1,3}+P_{3,1})^2\right]\\&+\frac{1}{2}G_{44}^{'}\left[(P_{1,2}-P_{2,1})^2+(P_{2,3}-P_{3,2})^2+(P_{1,3}-P_{3,1})^2\right]\end{aligned} \tag{8}$$

where G_{ij} are gradient energy coefficients. $P_{i,j}$ denote $\partial P_i/\partial r_j$. The gradient energy coefficients are chosen to be $G_{11}/G_{110} = 1.2$, $G_{12}/G_{110} = 0$, $G_{44}/G_{110} = G_{44}/G_{110} = 0.6$, where $G_{110} = 7.04 \times 10^{-11}C^{-}$ [2] m^4N. The time step for integration is $\Delta t/t_0 = 0.01$, where $t_0 = 1/\ L\alpha_1|_{T=300K}$. The corresponding elastic energy density can be expressed as:

$$f_{\text{elas}}=\frac{1}{2}c_{ijkl}e_{ij}e_{kl}=\frac{1}{2}c_{ijkl}\left(\varepsilon_{ij}-\varepsilon_{ij}^0\right)\left(\varepsilon_{kl}-\varepsilon_{kl}^0\right) \tag{9}$$

where c_{ijkl} is the elastic stiffness tensor, ε_{ij} the total strain, ε_{kl}^0 the electrostrictive stress-free strain, i.e., $\varepsilon_{kl}^0 = Q_{ijkl}P_kP_l$. The elastic constants and electrostrictive coefficients of $BaTiO_3$ are used in the simulations A semi-implicit Fourier-spectral method is adopted for numerically solving the TDGL equation. In the computer simulations, 2D 64 × 64 discrete grid points and 3D 64 × 64 × 64 discrete grid points are employed. The grid space in real space is chosen to be $\Delta x = \Delta y = \Delta z = 1$ nm. Periodic boundary conditions are used to simplify numerical calculations.

Declaration of competing interest

The authors declare that they have no known competing financial interests or personal relationships that could have appeared to influence the work reported in this paper.

CRediT authorship contribution statement

Dawei Wang: Investigation, Methodology, Conceptualization, Writing - original draft. **Zhongming Fan:** Investigation. **Guanghui Rao:** Resources, Writing - review & editing. **Ge Wang:** Validation. **Yao Liu:** Software. **Changlai Yuan:** Validation. **Tao Ma:** Investigation. **Dejun Li:** Resources, Writing - review & editing. **Xiaoli Tan:** Supervision. **Zhilun Lu:** Validation. **Antonio Feteira:** Writing - review & editing. **Shiyu Liu:** Software, Writing - original draft. **Changrong Zhou:** Resources, Supervision, Writing - review & editing. **Shujun Zhang:** Supervision, Writing - review & editing.

Acknowledgements

The authors acknowledge the funding and supporting from the Engineering and Physical Sciences Research Council (EP/L017563/1, EP/N010493/1) and National Natural Science Foundation of China (11564007, 61361007).

Appendix A. Supplementary data

Supplementary data to this article can be found online at https://doi.org/10.1016/j.nanoen.2020.104944.

References

[1] S. Zhang, et al., Prog. Mater. Sci. 68 (2015) 1.
[2] B. Jaffe, W.R. Cook, H. Jafe. Piezoelectric Ceramics, Academic, London, 1971.
[3] G.H. Haertling, J. Am. Ceram. Soc. 82 (4) (1999) 797.
[4] Directive 2002/95/EC of the European Parliament and of the Council of 27 January 2003 on the restriction of the use of certain hazardous substances in electrical and electronic equipment, Official Journal of the European Union 13 (2003) 2.
[5] T.R. Shrout, S.J. Zhang, J. Electroceram. 19 (1) (2007) 113.
[6] J. Rödel, et al., J. Am. Ceram. Soc. 92 (6) (2009) 1153.
[7] D. Wang, et al., J. Adv. Dielectrics (2018), 1830004.
[8] D.W. Wang, et al., J. Eur. Ceram. Soc. 37 (4) (2017) 1857.
[9] D.W. Wang, et al., ACS Appl. Energy Mater. 1 (8) (2018) 4403.
[10] D.W. Wang, et al., J. Mater. Chem. 6 (9) (2018) 4133.
[11] S. Murakami, et al., J. Eur. Ceram. Soc. 38 (12) (2018) 4220.
[12] S. Murakami, et al., J. Am. Ceram. Soc. 101 (12) (2018) 5428.
[13] S. Chandarak, et al., J. Supercond. Nov. Magnetism 26 (2) (2012) 455.
[14] Y. Saito, et al., Nature 432 (7013) (2004) 84.
[15] K. Xu, et al., Adv. Mater. 28 (38) (2016) 8519.
[16] D.W. Wang, et al., J. Am. Ceram. Soc. 100 (2) (2017) 627.
[17] Q. Liu, et al., Energy Environ. Sci. 11 (12) (2018) 3531.
[18] T. Zheng, et al., Energy Environ. Sci. 10 (2) (2017) 528.
[19] K. Xu, et al., Adv. Mater. 28 (38) (2016) 8519.
[20] W.F. Liu, X.B. Ren, Phys. Rev. Lett. 103 (25) (2009).
[21] M.H. Lee, et al., Adv. Mater. 27 (43) (2015) 6976.
[22] F. Li, et al., Science 364 (6437) (2019) 264.
[23] F. Li, et al., Nat. Mater. 17 (4) (2018) 349.
[24] M.J. Haun, et al., Ferroelectrics 99 (1989) 13.
[25] H.X. Fu, R.E. Cohen, Nature 403 (6767) (2000) 281.
[26] D. Damjanovic, IEEE Trans. Ultrason. Ferroelectr. Freq. Control 56 (8) (2009) 1574.
[27] S.M. Neirman, J. Mater. Sci. 23 (11) (1988) 3973.
[28] F. Li, et al., Adv. Funct. Mater. 28 (37) (2018), 1801504.
[29] L.E. Cross, Ferroelectrics 76 (1) (1987) 241.
[30] M. Deluca, et al., J. Mater. Chem. 6 (13) (2018) 5443.
[31] C.L. Zhao, et al., J. Am. Chem. Soc. 140 (45) (2018) 15252.
[32] Z.M. Wang, et al., J. Mater. Sci. Mater. Electron. 27 (5) (2016) 5047.
[33] H.J. Sun, et al., J. Alloys Compd. 670 (2016) 262.
[34] R.H. Yuan, et al., Adv. Mater. 30 (7) (2018).
[35] M. Acosta, et al., Appl. Phys. Rev. 4 (4) (2017).
[36] D. Berlincourt, Piezoelectric crystals and ceramics, in: Ultrasonic Transducer Materials, Springer, 1971, p. 63.
[37] T. Ma, et al., Phys. Rev. Lett. 123 (21) (2019) 217602.
[38] W. Kohn, L.J. Sham, Phys. Rev. 140 (4A) (1965) A1133.
[39] P. Hohenberg, W. Kohn, Phys. Rev. 136 (3B) (1964) B864.
[40] M. Segall, et al., J. Phys. Condens. Matter 14 (11) (2002) 2717.
[41] J.P. Perdew, et al., Phys. Rev. Lett. 77 (18) (1996) 3865.
[42] S.-Y. Liu, et al., Phys. Chem. Chem. Phys. 19 (33) (2017) 22190.
[43] S.Y. Liu, et al., J. Am. Ceram. Soc. 99 (10) (2016) 3336.
[44] L.Q. Chen, J. Am. Ceram. Soc. 91 (6) (2008) 1835.
[45] F. Li, et al., Nat. Commun. 7 (2016) 13807.
[46] Y Yao, et al., EPL 98 (2012) 27008.
[47] N Horchidan, et al., J. Eur. Ceram. Soc. 34 (2014) 3661–3674.

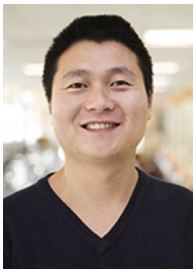

Dawei Wang is a Research Associate at MSE of the University of Sheffield since 2014. He received his PhD degree from Beijing Institute of Technology in 2012. He was also a Joint PhD student and a visiting scholar at the MRI of Pennsylvania State University. His research focuses on the synthesis and characterization of innovative energy storage/conversion/harvesting materials, and translation of new materials to prototype devices/components. He holds 5 issued patents and has published 100+ papers, with a google scholar citation of 2400+ and H-index of 31. He is an associate editor for Journal of American Ceramic Society.

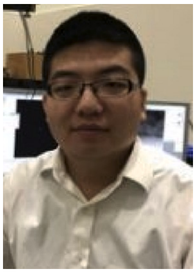

Zhongming Fan is currently a postdoctoral research associate in Material Research Institute (MRI) at Pennsylvnia State University. He received his Ph. D degree from Iowa State University in 2019. His research interests include electrical measurements and TEM characterization on lead-free piezoelectric ceramics.

Guanghui Rao is currently a Bagui scholar of Province and a full Professor at the School of Materials Science and Engineering, Guilin University of Electronic Technology (GUET), Guangxi, China. He received his MSc degree (1985) and PhD degree (1988) in Condensed Matter Physics from the Institute of Physics (IOP), Chinese Academy of Sciences, and then worked in the same Institute. He was a full professor of physics and a research group leader at IOP before joining the GUET in 2011. His research focuses on crystallography, phase transition and structure-property relationships of functional materials.

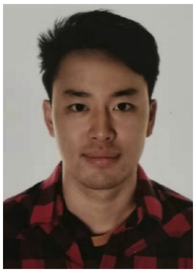

Ge Wang is currently working as a PDRA in the functional materials and devices group at the University of Sheffield, UK. He obtained his PhD degrees in electroceramics at the University of Manchester in 2017. His research interests focused on investigation structure-composition-properties relationships in electroceramics, including dielectrics, ferroelectrics and piezoelectrics. He also experienced in fabrication layered-structure prototype devices for multilayer ceramic capacitors, solid oxide fuel cell and Li batteries.

Yao Liu is a Ph.D. candidate of electronic science and technology at Xi'an Jiaotong University, China. He received the B.E. degree in electronic science and technology from Xi'an Jiaotong University. His research focuses on computational simulations of piezoelectrics.

Changlai Yuan is currently a full Professor at the School of Materials Science and Engineering, Guilin University of Electronic Technology (GUET), Guangxi, China. He received his PhD degree (2012) in College of Material Science and Engineering, Central South University, China. His research focuses on ferroelectric, energy storage and microwave dielectric properties of functional materials.

Tao Ma is a staff scientist in the Michigan Center for Materials Characterization (MC) [2] at University of Michigan and previously worked as a postdoctoral research associate at the Ames Laboratory. He received his Ph.D. degree from Hokkaido University in 2013. His research is focused on microscopic characterization of functional and energy conversion materials via electron microscopy.

Dejun Li is a distinguished Professor at College of Physics and Materials Science, Tianjin Normal University, China. He received his doctor degree from Tsinghua University, China, in 1999. His main research interests include nano-multilayer films, thin solid films, carbon-based materials, superhard materials, biomedical materials and energy storage materials. He has authored and co-authored more than 200 papers. He holds more than 20 Chinese patents and has presented over 20 invited talks in international academic conferences.

Xiaoli Tan is a Professor of Materials Science and Engineering in Iowa State University (ISU). He received his Ph. D degree from University of Illinois at Urbana-Champaign and joined ISU in 2002. His group applies various TEM techniques (HRTEM, in-situ biasing/stress/heating) to the study of a broad range of physical phenomena in electroceramics, e.g. dielectric breakdown, ferroelectric fatigue and ferroic phase transformation.

Zhilun Lu obtained his Ph.D. from the Department of Materials Science and Engineering at the University of Sheffield, on January 2016 with the High-Quality PhD Thesis Prize. He worked as a research beam scientist in Helmholtz-Zentrum Berlin before joining The Henry Royce Institute and Department of Materials Science and Engineering at the University of Sheffield. His work focuses on inventing innovative functional and energy materials with expertise in synthesis, structural and property characterization, as well as coordinating development, and covers a wide range of functional ceramics (energy storage capacitors, thermoelectrics, dielectrics, high permittivity oxides, microwave and geometrically frustrated magnets).

Antonio Feteira is currently a Professor of Advanced funtional Materials in the Department of Engineering and Mathematics at Sheffield Hallam University. He received his PhD degree in Materials Science and Engineering from The University of Sheffield, where he holds a visiting position. In the past, he was a Senior Research Fellow at the University of Birmingham, having previously worked in the R&D department of TDK EPC, Austria. He held visiting research positions at Penn State University, Warwick University, Max Planck Institute, Complutense University of Madrid. His research focuses on advanced ceramics for electronics, including actuators, energy storage devices, temperature sensors and wireless communication resonators.

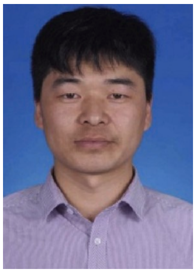

Shiyu Liu is an Associate Professor at College of Physics and Materials Science, Tianjin Normal University, China. Liu received his PhD degree from Beihang University, China, in 2010. He was a visiting scientist in 2014 at Prof. Yaogen Shen's Group at City University of Hong Kong. His current research interests include first-principles calculation, relaxor ferroelectrics, antiferroelectrics, lead-free piezoceramics, ultrahigh temperature ceramics; energy storage materials, superconductors and Landau thermodynamics theory.

Changrong Zhou is currently a Professor at the School of Materials Science and Engineering, Guilin University of Electronic Technology (GUET), Guangxi, China. He received his B.S. and M. S. and Ph.D. degree in materials science and engineering from Central South University, Changsha, China, in 1998, 2004 and 2008, respectively. He visited University of Birmingham during 2010–2011 as a visiting scholar. His research is focused on ferroelectric and piezoelectric materials.

Shujun Zhang is a Professor at ISEM/AIIM of UOW, prior to which, he was a Professor at MatSE Department and Senior Scientist at MRI of PSU. He is associate EIC of IEEE Transaction UFFC; associate editor of Science Bulletin; Journal ACerS and Journal Electronic Materials, section EIC of Crystals. He is fellow of ACerS and senior member of IEEE, elected AdCom member of IEEE-UFFC. He is now focusing on fabrication-microstructure-property-performance relationship of functional materials for piezoelectric sensor, transducer and energy storage/harvesting applications.